Medical Engineering and Physics 000 (2017) 1–12

Contents lists available at ScienceDirect

Medical Engineering and Physics

journal homepage: www.elsevier.com/locate/medengphy

A framework for computational fluid dynamic analyses of patient-specific stented coronary arteries from optical coherence tomography images

Susanna Migliori[a], Claudio Chiastra[a], Marco Bologna[a,b], Eros Montin[b], Gabriele Dubini[a], Cristina Aurigemma[c], Roberto Fedele[d], Francesco Burzotta[c], Luca Mainardi[b], Francesco Migliavacca[a,*]

[a] Laboratory of Biological Structure Mechanics (LaBS), Department of Chemistry, Materials and Chemical Engineering "Giulio Natta", Politecnico di Milano, Milan, Italy
[b] Department of Electronics, Information and Bioengineering, Politecnico di Milano, Milan, Italy
[c] Institute of Cardiology, Catholic University of the Sacred Heart, Rome, Italy
[d] Department of Civil and Environmental Engineering, Politecnico di Milano, Milan, Italy

ARTICLE INFO

Article history:
Received 20 February 2017
Revised 9 June 2017
Accepted 16 June 2017
Available online xxx

Keywords:
Optical coherence tomography
X-ray computed micro tomography
Image segmentation
Coronary artery
Stent
Computational fluid dynamics

ABSTRACT

The clinical challenge of percutaneous coronary interventions (PCI) is highly dependent on the recognition of the coronary anatomy of each individual. The classic imaging modality used for PCI is angiography, but advanced imaging techniques that are routinely performed during PCI, like optical coherence tomography (OCT), may provide detailed knowledge of the pre-intervention vessel anatomy as well as the post-procedural assessment of the specific stent-to-vessel interactions. Computational fluid dynamics (CFD) is an emerging investigational tool in the setting of optimization of PCI results. In this study, an OCT-based reconstruction method was developed for the execution of CFD simulations of patient-specific coronary artery models which include the actual geometry of the implanted stent.

The method was applied to a rigid phantom resembling a stented segment of the left anterior descending coronary artery. The segmentation algorithm was validated against manual segmentation. A strong correlation was found between automatic and manual segmentation of lumen in terms of area values. Similarity indices resulted >96% for the lumen segmentation and >77% for the stent strut segmentation. The 3D reconstruction achieved for the stented phantom was also assessed with the geometry provided by X-ray computed micro tomography scan, used as ground truth, and showed the incidence of distortion from catheter-based imaging techniques. The 3D reconstruction was successfully used to perform CFD analyses, demonstrating a great potential for patient-specific investigations.

In conclusion, OCT may represent a reliable source for patient-specific CFD analyses which may be optimized using dedicated automatic segmentation algorithms.

1. Introduction

Coronary heart diseases (CHDs) are the major causes of death in the Western Countries [1,2]. The principal source of CHD is the narrowing of vessel lumen because of atherosclerotic plaque development. The most widely performed CHD surgical treatment is percutaneous coronary intervention (PCI), due to the reduced hospitalization, recovery time and costs [2]. The influence of coronary anatomy on PCI outcomes is largely confirmed [3]. Consequently, the significant anatomic variability observed among individuals has led to an increasing application of intravascular imag-

Abbreviations: CAD, computer-aided design; CFD, computational fluid dynamics; CHD, coronary heart disease; DICOM, digital imaging and communications in medicine; FN, false negatives; FP, false positives; ISR, in-stent restenosis; IVUS, intravascular ultrasound; LAD, left anterior descending; MB, main branch; µCT, micro computed tomography; OCT, optical coherence tomography: PCI, percutaneous coronary intervention; SB, side branch; TAWSS, time-averaged wall shear stress; TN, true negatives; TP, true positives.

* Corresponding author.
E-mail addresses: susanna.migliori@polimi.it (S. Migliori), francesco.migliavacca@polimi.it (F. Migliavacca).

http://dx.doi.org/10.1016/j.medengphy.2017.06.027

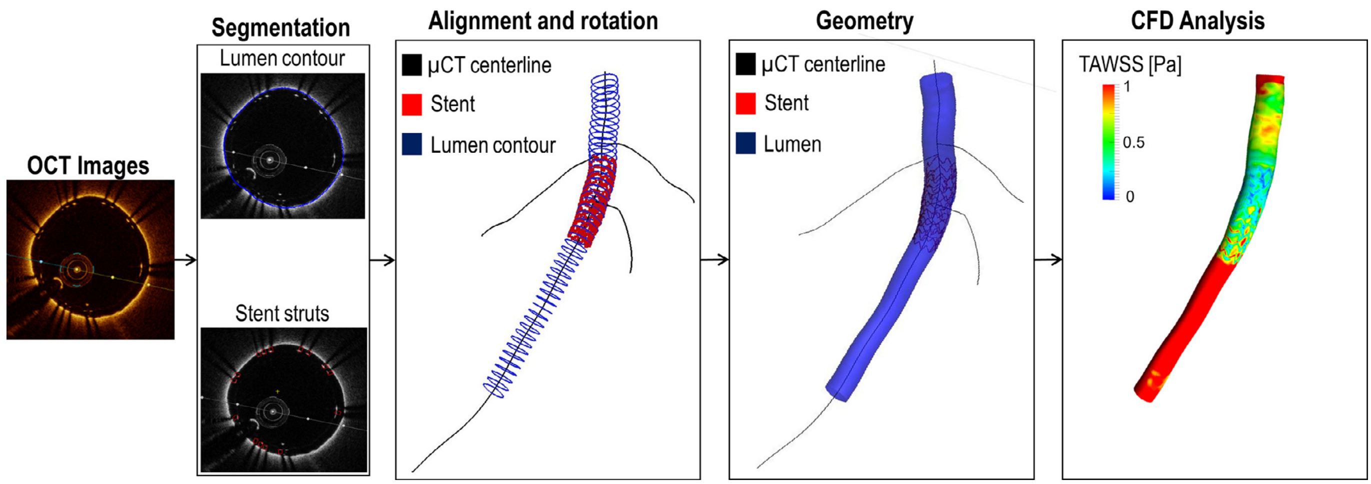

Fig. 1. General workflow of the proposed methodology, suitable for the 3D reconstruction of a stented coronary phantom from optical coherence tomography (OCT) images and the subsequent execution of computational fluid dynamics analyses. In the box on the right, the contour map of time-averaged wall shear stress (TAWSS) is shown.

ing techniques for the characterization of each specific clinical case [4,5]. The present investigation, alongside the application of advanced computational simulation tools, potentially enables the prediction of long-term outcomes of planned or applied treatments [6]. Among the possible vascular responses to PCI, in-stent restenosis (ISR) is one of the most frequent [7]. The origin of ISR is not completely understood. However, it has been demonstrated that the alterations of local hemodynamics due to stent insertion play an important role on the onset of ISR [8]. In fact, the stent affects the local flow patterns by determining non-physiological recirculation or stagnation areas and altered distribution of wall shear stress [9,10], which can induce and promote ISR [8].

Coronary artery imaging is largely performed both during diagnostic phase and surgical treatment [11–13]. Optical coherence tomography (OCT) is a catheter-based imaging intravascular technique that uses light with a bandwidth within the near-infrared spectrum [14]. The vessel inside is imaged by multiple axial scans (A-scans) that are performed in a spiral-like manner by the OCT probe. This imaging modality ensures higher image resolution compared to that provided by ultrasound-based methods (i.e. intravascular ultrasound—IVUS), with axial resolution ranging from 12 to 18 µm (against 150 to 200 µm of IVUS) and lateral resolution ranging from 20 to 90 µm (against 150 to 300 µm of IVUS) [14]. Therefore, OCT is more and more used to guide PCI by providing information on atherosclerotic plaque extension and composition, and by monitoring stent positioning [15,16]. The main drawback of OCT is the fact that it lacks of information on the 3D shape of the analyzed coronary segment. Consequently, information from other techniques is needed to reconstruct the geometry of the treated blood vessel [13,17–19].

In the present study, we propose an OCT-based reconstruction method of patient-specific coronary artery models, which includes the actual geometry of the implanted stent, for the execution of computational fluid dynamic (CFD) simulations (Fig. 1). To assess the novel methodology, the following workflow was conceived. A representative geometry of a human left anterior descending (LAD) coronary artery was 3D printed as a rigid phantom in which a stent was expanded. This phantom was then used to develop and validate the reconstruction method (Fig. 2). OCT images of the phantom were segmented to identify lumen contour and stent struts. These components were aligned and orientated with the centerline of the phantom 3D reconstruction realized from X-ray computed micro tomography (µCT) scan. The accuracy of the reconstruction method was evaluated in both the image segmentation and the alignment/orientation processes. The former was validated against manual segmentation of OCT images where two image readers identified the region of interest for the lumen and the stent. The latter was assessed by comparing the outcomes obtained for the lumen and the stent with the reconstruction from µCT scan.

2. Material and methods

2.1. Coronary artery phantom and image acquisition

A rigid phantom emulating a typical human LAD artery with multiple bifurcations was designed using the computer-aided design (CAD) software Rhinoceros v. 5.0 (Robert McNeel & Associates, Seattle, WA, USA). A cavity within a solid block comprising one main branch (MB) and three side branches (SBs) was realized (Fig. 2A). The main sizes of the phantom were 37.4 mm, 53.8 mm, and 32.8 mm; the MB was 64 mm long with diameters at inlet and outlet of 3.5 mm and 2.8 mm, respectively. The phantom was printed using a commercially available resin, DM220 Moulding Resin (DWS, Italy), through a DWS028JPlus stereo-lithography apparatus (DWS, Italy) (Fig. 2B) [20]. A Multi-Link 8 stent (Abbott Laboratories, Abbott Park, IL, USA) (diameter = 3.5 mm, length = 12 mm) was deployed by an interventional cardiologist following a standard stenting procedure (Fig. 2C). In particular, the coronary stent was deployed in the MB by balloon inflation at 16 atm for 20 s. Then, post-dilation was performed by inflating a balloon (diameter = 3.5 mm, length = 12 mm) at 16 atm at the stent proximal segment to limit malapposition.

OCT images were acquired in the MB using the commercially available C7-XR Fourier-Domain OCT system (St. Jude Medical, St. Paul, MN, USA) with a C7 Dragonfly catheter (St. Jude Medical) (Fig. 2D). Length of the analyzed segment was 54 mm and the automated pull-back speed was 18 mm/s resulting in a data frame rate of 180 frames per second. The OCT acquisition system ensured axial and lateral resolutions of 12–18 µm and 20–90 µm, respectively. The image set accounted for 540 frames with a distance between frames of 100 µm and each OCT frame was recorded in DICOM format with dimension of 1024 × 1024 pixels.

The phantom was also scanned with a X-ray µCT NSI X25 system (NSI Inc., Rogers, MN, USA), equipped with a Dexela detector with 75 µm pixel pitch allowing for the acquisition of 1536 × 1944 pixel radiographies at full-binning with 16 bit encoding (Fig. 2F) [20]. Details on this imaging technique, recently en-

Please cite this article as: S. Migliori et al., A framework for computational fluid dynamic analyses of patient-specific stented coronary arteries from optical coherence tomography images, Medical Engineering and Physics (2017), http://dx.doi.org/10.1016/j.medengphy.2017.06.027

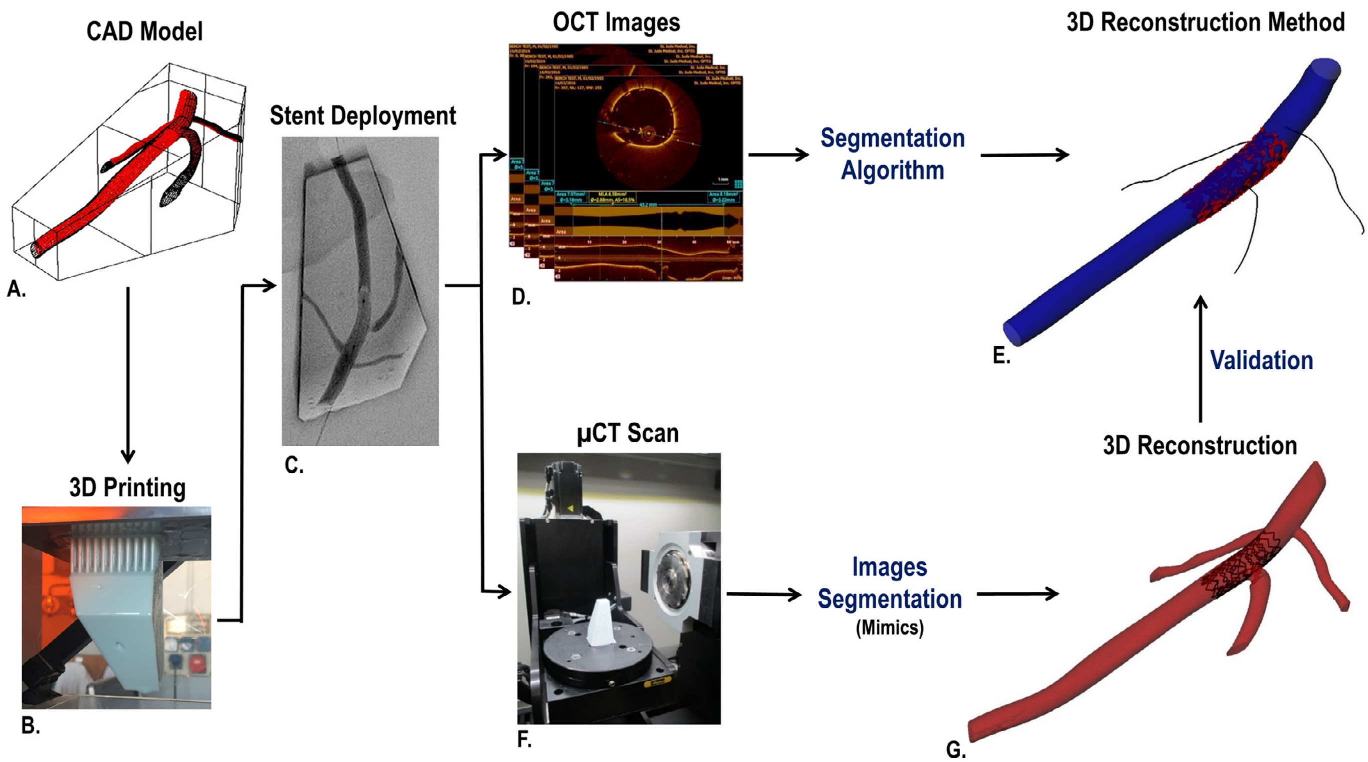

Fig. 2. Workflow followed to validate the developed reconstruction method. (A) Computer-aided design (CAD) model of the phantom resembling a human left anterior descending coronary artery with multiple bifurcations. (B) Printing of 3D phantom. (C) Angiography of the phantom after stent deployment. (D) Optical coherence tomography (OCT) applied to the phantom after stent deployment. (E) 3D reconstruction of the phantom main branch achieved with the present method. (F) X-ray micro computed tomography (μCT) scan system. (G) 3D reconstruction from μCT data of the phantom by means of a commercial software.

riched with in situ loading apparata and image processing algorithms for in bulk strain assessment, can be found in Fedele et al. [21–23]. The obtained μCT slices were post-processed with Mimics software (Materialise, Leuven, Belgium) to extract the vessel and stent centerlines.

2.2. Method for three-dimensional reconstruction

The proposed 3D reconstruction method entirely runs in a MATLAB environment (Mathworks, Natick, MA, USA) and consists of four stages: (i) image pre-processing, (ii) lumen contour detection, (iii) stent struts detection, and (iv) alignment and orientation of detected lumen contours and stent struts with the vessel centerline. The reconstruction method is described in the following subsections. Additional details about the first three stages can be found in Chiastra et al. [24].

2.2.1. Image pre-processing

First, each OCT frame (Figs. 3A and 4A) is converted from RGB color mode to grayscale and the line dividing the two vessel visualization modalities (i.e. cross-sectional and longitudinal views) is used to isolate the vessel cross-section. Second, pixels belonging to the OCT visualization tools (i.e. calibration bar, scale, and other information related to the image) are removed. The implemented approach is founded on the fact that such pixels have both same intensity and position across frames. Consequently, their grayscale intensity is forced to zero.

The processed images are converted in polar coordinates for further elaborations (Figs. 3B–E and 4B–E). This procedure aims to express the position of each pixel in an image through radial and angular coordinates that are centered on the OCT catheter. Indeed, a dataset generated from OCT pullback is coaxial to the catheter and the infrared light is radially emitted from the OCT probe (A-scan). Therefore, the catheter covers a region at the top of the image in polar coordinates and it is deleted by image global thresholding at a selected image portion. That region is defined taking into account the catheter radius, image resolution, and the highest values of average intensity. The border of the catheter region, ρ_{lim}, is estimated as the last line of pixels with an intensity higher than an imposed threshold (i.e. quantile 95%) on the average intensity. Consequently, the catheter is considered a circle with a radius of $\rho_{\text{cat}} = \rho_{\text{lim}} + 10$, which includes a tolerance of 10 pixels. Once the OCT catheter region is identified in each image, a first rough removal is performed by forcing to zero all pixels with intensity above the imposed threshold. A finer catheter removal is performed through the search for background pixels (intensity below the quantile 75% in the histogram) across image columns (A-scans) within the filtered region. Thus, when a background pixel is found, all the previous image lines are forced to zero, so that the lumen contour is preserved where it is in contact with the catheter during OCT pullback.

2.2.2. Detection of lumen contour

Regions with higher intensity pixels are isolated in order to remove noise and to depict the lumen contour portion. The salt-and-pepper noise is removed from each image by applying an intensity thresholding followed by other morphological operations [25], including area thresholding and opening. The obtained binary mask is convolved over the grayscale image (Fig 3C).

A first edge detection is performed by means of a Sobel operator [25]. Particularly, this operator computes the gradient of a function and identifies borders within an image. Thus, the first non-zero element found in each column of the filtered image in polar coordinates is accepted as a valid point for the lumen border.

Since the resultant images might have been affected by either residual noise or bifurcation regions, a post-processing phase is

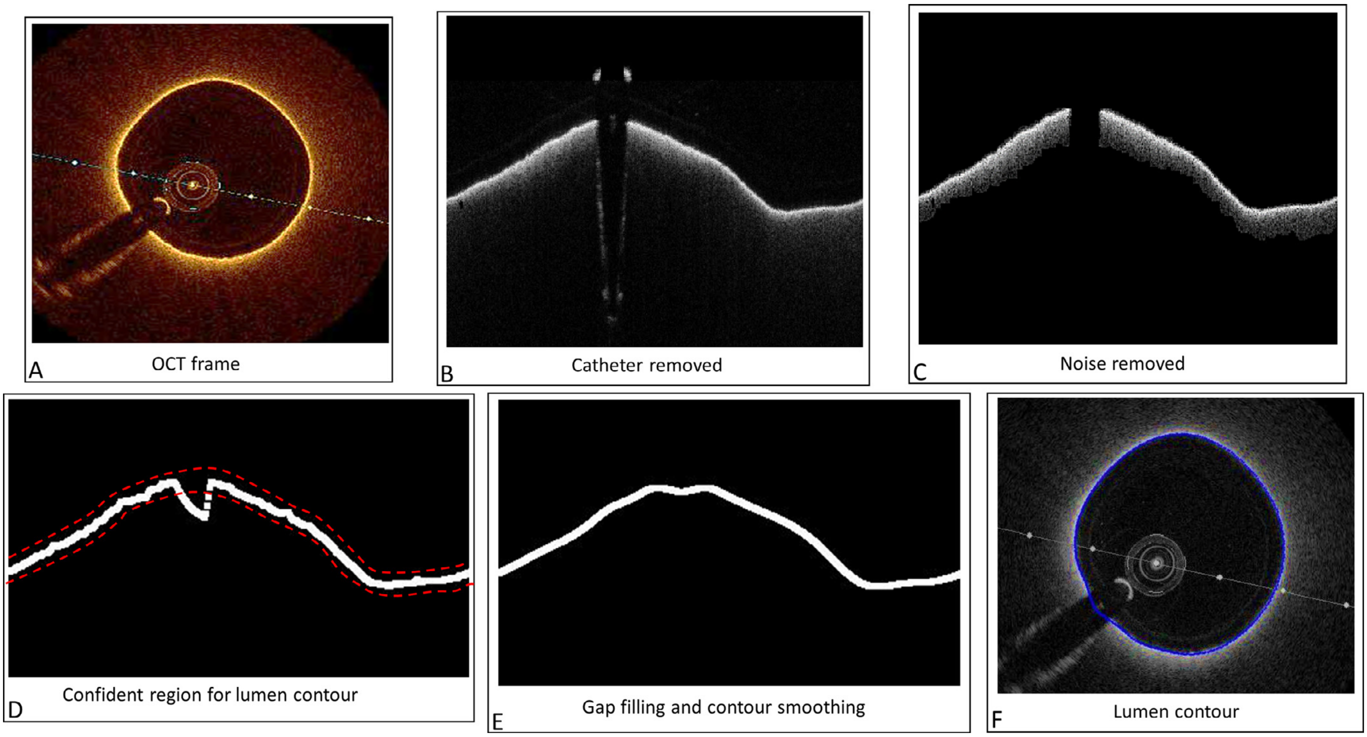

Fig. 3. Lumen contour detection based on segmented images from optical coherence tomography (OCT). (A) Cross-sectional visualization of an OCT frame. (B) Grayscale image in polar coordinates after removal of the OCT catheter. (C) Masked image after noise removal. (D) Binary image in polar coordinates with the identified lumen contour (a dilatation of 2 pixels has been applied to enable the edge visualization) and schematic representation of the confidence region (red dashed line). (E) Binary image in polar coordinates of the lumen contour (a dilatation of 2 pixels has been applied to enable the edge visualization) after gap filling and contour smoothing. (F) Grayscale image of the cross-sectional visualization with the identified lumen contour (blue). (For interpretation of the references to colour in this figure legend, the reader is referred to the web version of this article.)

included for error correction. The implemented strategy is based on the assumption that the lumen maintains its shape between consecutive frames. Therefore, in the current image a confidence region is defined from the contour pixels found in the previous one with a tolerance of ±5 pixels (Fig. 3D). Points outside that range are deleted and the image is then filtered to remove small objects.

Resultant gaps along the lumen edge are filled either by linear interpolation or by replicating contour pixels from previous OCT frames. In particular, the strategy is chosen depending on the gap amplitude in terms of number of columns with only zero elements. The detected lumen contours are smoothed with a moving average filter (Fig 3E). Finally, images are converted back in Cartesian coordinates and lumen contours are recorded as points in the 2D plane (Fig 3F).

2.2.3. Detection of stent struts

Detection of metallic stent struts is achieved through the peculiar characteristic of OCT images, where stent struts appear as high reflecting elements (i.e. high intensity region) followed by a trailing shadow (i.e. low intensity region) (Fig 4B) [26]. Therefore, the intensity profile of each A-scan in the OCT frame is considered in order to estimate struts position. The slope of a line connecting each peak in the intensity profile with the thirtieth consecutive low intensity pixel is computed and pixels that result in higher slope values are considered part of a strut [27]. Columns corresponding to the A-scans that do not cross a candidate stent strut are set to zero. Then, the obtained grayscale images are processed to isolate regions with higher intensity pixels and whose extension is below a certain number of rows, according to the strut thickness (i.e. 10 rows). Lastly, the first sets of high intensity pixels are considered for the following processes.

A fuzzy logic approach is applied to identify strut pixel and delete false positives (Fig. 4D). In particular, a mask is created to reflect the probability that a pixel in the image belongs to a strut. The mask is a grayscale image with intensity values from 0 to 1 moving from the lumen center toward the lumen contour and 0 below it.

The obtained images are elaborated with a confidence region that is defined by merging information provided by previous and successive five images in order to build a smooth curve. Points that are above a tolerance of ±5 pixels are deleted (Fig. 4E).

At the end of the procedure, each image is converted back to Cartesian coordinates. The centroids of regions with white pixels provide the position of stent struts (Fig. 4F), recorded as points in the 2D plane.

2.2.4. Alignment and orientation of detected components

The detected lumen contours and stent struts are aligned with the centerline of the artery phantom extracted after µCT scan (Fig. 2G). This enables quantitative comparison between the reconstruction achieved with the proposed methodology and the reference geometry. The MB vessel centerline is sampled by assuming the same distance between consecutive frames as acquired on the OCT catheter. Such an assumption ensures a correspondence between each point on the MB centerline and each OCT frame. The alignment method includes the superimposition of lumen contours on the corresponding vessel centerline point and, subsequently, the orientation according to Frenet–Serret formulas (Eq. (1)) [12], which resemble the alignment of OCT frames perpendicularly to the curve, as shown in Fig. 5A. In particular, in Eq. (1) the three right-handed orthonormal vectors, i.e. tangential ($\boldsymbol{T}$), normal ($\boldsymbol{N}$) and binormal ($\boldsymbol{B}$), to a space curve (c) are defined as function of the arc length (s). The curvature (k) and torsion (τ) are

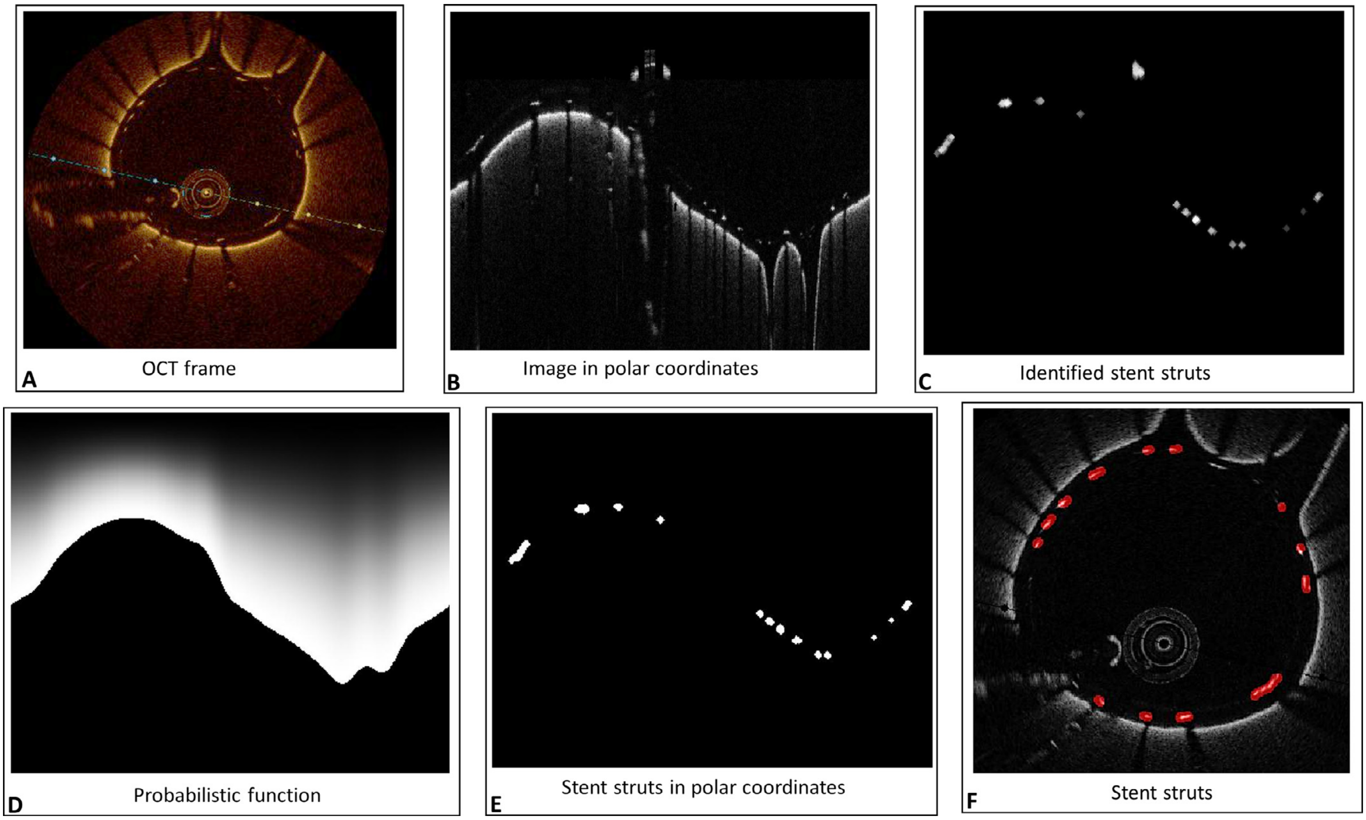

Fig. 4. Stent struts detection through optical coherence tomography (OCT) segmented images. (A) Cross-sectional visualization of an OCT frame with stent struts. (B) Grayscale image in polar coordinates after removal of the OCT catheter. (C) Masked image after noise removal. (D) Grayscale image of the probabilistic function defined for removal of false positives. (E) Binary image in polar coordinates of the stent struts (a dilatation of 2 pixels has been applied to better the visualization). (F) Grayscale image of the cross-sectional visualization with the identified stent struts (red). (For interpretation of the references to colour in this figure legend, the reader is referred to the web version of this article.)

$k = \|c''(s)\|$ and $\tau = \det[c'(s), c''(s), c'''(s)]/k^2(s)$, respectively:

$$\begin{aligned} \frac{d\boldsymbol{T}}{ds} &= k\boldsymbol{N}, \\ \frac{d\boldsymbol{N}}{ds} &= -k\boldsymbol{T} + \tau\boldsymbol{B} \\ \frac{d\boldsymbol{B}}{ds} &= -\tau\boldsymbol{N} \end{aligned} \tag{1}$$

In order to reduce the axial twist angle error that generally rises from intravascular imaging techniques [28], the centerline of one SB is chosen as the landmark for twist angle estimation. That choice is driven by the quality of the acquired OCT frames concerning the degree of distinction between MB and SB at the carina. A marker for the chosen SB is manually selected on an OCT frame that corresponds to the middle of the bifurcation region so that the twist angle is computed to superimpose the marker on the SB centerline (Fig. 5B). The whole set of detected components is rotated according to that estimated angle.

Two point clouds are obtained from the alignment and orientation procedure, one for the lumen contours and one for the struts centroids, then used to define a geometry for subsequent CFD analyses.

2.3. Validation of the reconstruction method

2.3.1. Segmentation algorithm

Results from the segmentation algorithm were assessed through a manual segmentation, which was considered as the reference. The manual segmentation was performed using the open-source software MRIcro (http://www.mccauslandcenter.sc.edu) by two independent expert image readers. Lumen contours were manually traced on 1 OCT frame out of 5, for a total of 95 frames, whereas stent struts were manually identified on the entire OCT dataset of the stented vessel portion, which included 122 frames.

The selected region-of-interest for the lumen was used to compute area values. The correlation between data sets was verified through the Kruskal–Wallis test, Bland–Altman analysis [29], and linear regression. Discrepancies between the automatic and manual segmentation methods were assessed by means of the computation of similarity indexes [30]. These indexes were defined by calculating the number of pixels that exhibited specific features, constituting the following subsets: true positives (TP—pixels that were labeled as lumen by both the segmentation methods), false positives (FP—those depicted only by the automatic segmentation), false negatives (FN—those identified by the manual segmentation), and true negatives (TN—pixels labeled as background by both the methods). Then, the selected similarity indexes were:

$$Jaccard\ index = \frac{TP}{TP + FP + FN} \tag{2}$$

$$Dice\ \ index = \frac{2{\cdot}TP}{2{\cdot}TP + FP + FN} \tag{3}$$

$$Sensitivity\ index = \frac{TP}{TP + FN} \tag{4}$$

$$Specificity\ index_{lumen} = \frac{TN}{FP + TN} \tag{5}$$

The similarity indexes computed for the stent were defined by evaluating the accuracy of the automatic segmentation for the correct number of detected stent struts at each OCT frame. The Jaccard index, Dice index, and Sensitivity index were computed using

Please cite this article as: S. Migliori et al., A framework for computational fluid dynamic analyses of patient-specific stented coronary arteries from optical coherence tomography images, Medical Engineering and Physics (2017), http://dx.doi.org/10.1016/j.medengphy.2017.06.027

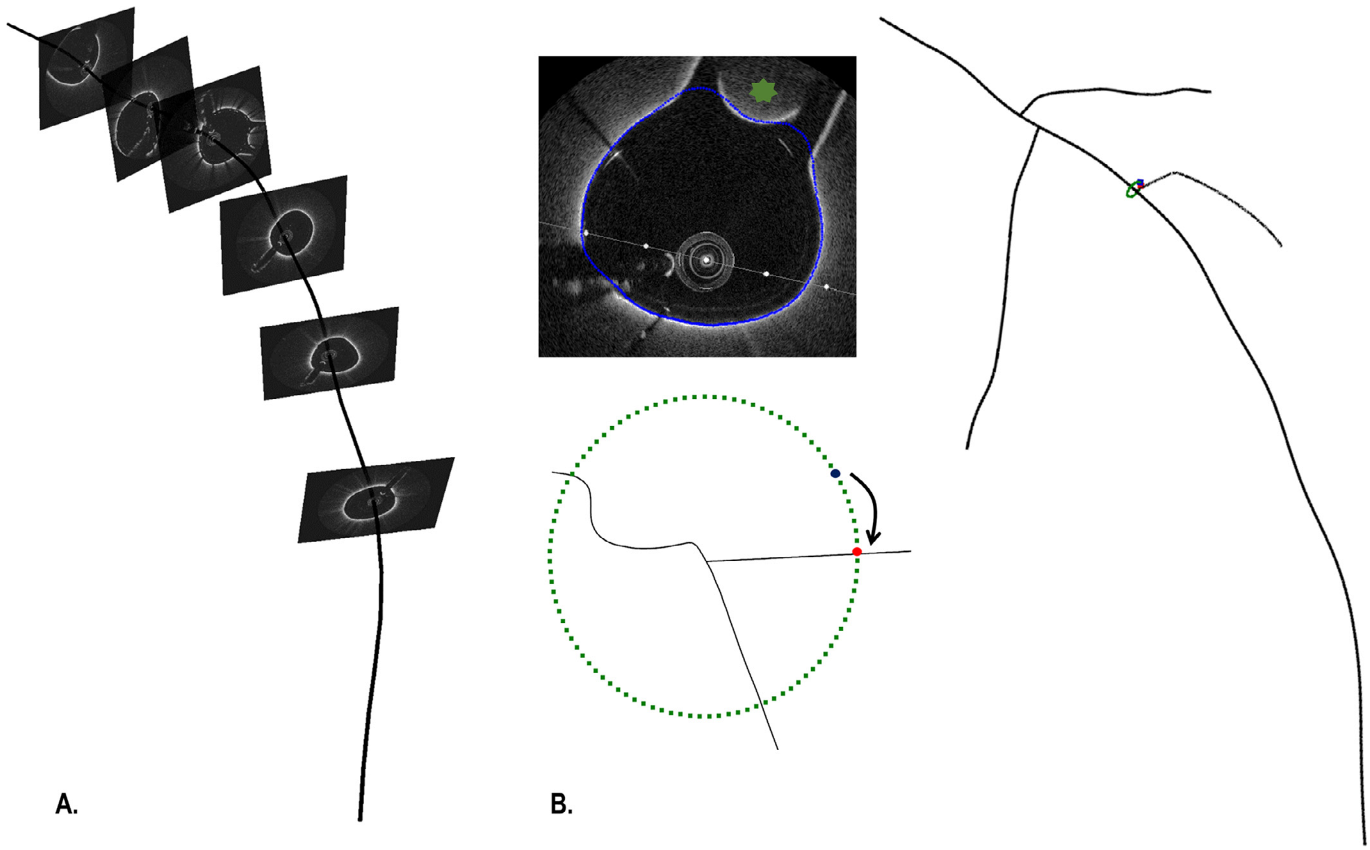

Fig. 5. (A) Alignment of optical coherence tomography (OCT) frames with the main branch centerline of the main branch. (B) Manual selection of a marker (green star) for the side branch chosen as landmark for rotation of the lumen contour (in blue) and stent. The rotation was needed to superimpose the marker (initial position in blue) on the side branch centerline (final position in red). (For interpretation of the references to colour in this figure legend, the reader is referred to the web version of this article.)

Eqs. (2)–(4). The specificity index was defined for stent as follows:

$$Specificity\ index_{stent} = \left(1 - \frac{FP}{n_{strut}}\right) \tag{6}$$

Moreover, correlation between the number of stent struts that were identified with the two segmentation methods was assessed through a Kruskal–Wallis test and the length of apposition (LOA) that is defined as the radial distance between a strut and the lumen contour [31]. The agreement between the data sets was evaluated with the Bland–Altman analysis.

2.3.2. Alignment and orientation method

The 3D lumen reconstruction, which was obtained with the proposed OCT-based method, was validated against that from µCT scan, used as a reference. In particular, the distance was evaluated between the lumen surface of the OCT and that from the µCT reconstruction. Then, the surface area that corresponded to a distance larger than 0.25 mm between the two reconstructions was calculated [18]. The relative error between the OCT and µCT reconstructions in terms of lumen volume was also computed. Furthermore, the point cloud for the stent obtained from OCT was compared with the stent centerline points from µCT by calculating the total distances between corresponding points.

2.4. Fluid dynamic model

2.4.1. 3D geometry

The lumen surface was reconstructed starting from the aligned point cloud of the lumen contours. Lumen contour points were automatically interpolated in curves that were used for lofting.

The 3D stent geometry was reconstructed starting from the obtained point cloud of the stent struts using a morphing procedure (Fig. 6A). The centerline of a free expanded 3.5 × 12 mm Multi-Link 8 stent (straight configuration) was extracted from µCT slices following the same procedure adopted for the phantom. The straight stent centerline was morphed into the deployed stent configuration using Hypermesh (Altair Engineering, Inc., Troy, MI, USA). Handles for mesh morphing were created on the centerline and moved to points that belong to the stent point cloud so that their distance was minimized (Fig. 6B). The morphed centerline was imported in Rhinoceros and the 3D geometry of the stent was achieved by means of the graphical algorithm editor Grasshoper® (www.grasshopper3d.com). In particular, the final stent geometry was obtained by positioning cross-section curves (i.e. squares with sides of 81 µm as the Multi-Link 8 stent strut cross-sections) on each ring and bridge (Fig. 6C) that were used for lofting.

The final 3D reconstructed model including the MB lumen and the stent is shown in Fig. 7.

2.4.2. CFD analysis

The 3D reconstruction was used to perform a proof-of-concept hemodynamic analysis on the actual LAD configuration after stent deployment (Fig. 1). The fluid domain was discretized using 3,234,032 tetrahedral elements by means of ANSYS ICEM CFD v.16 (ANSYS Inc., Canonsburg, PA, USA).

The transient CFD analysis was performed using ANSYS Fluent v.16 (ANSYS Inc.). A typical human LAD flow waveform [32] was applied with a flat velocity profile at the inlet cross-section [33]. Its mean value in time was defined so that the flow-rate was 45.15 ml/min, in agreement with [34]. At the outlet cross-section a zero pressure condition was set. No slip-condition was applied

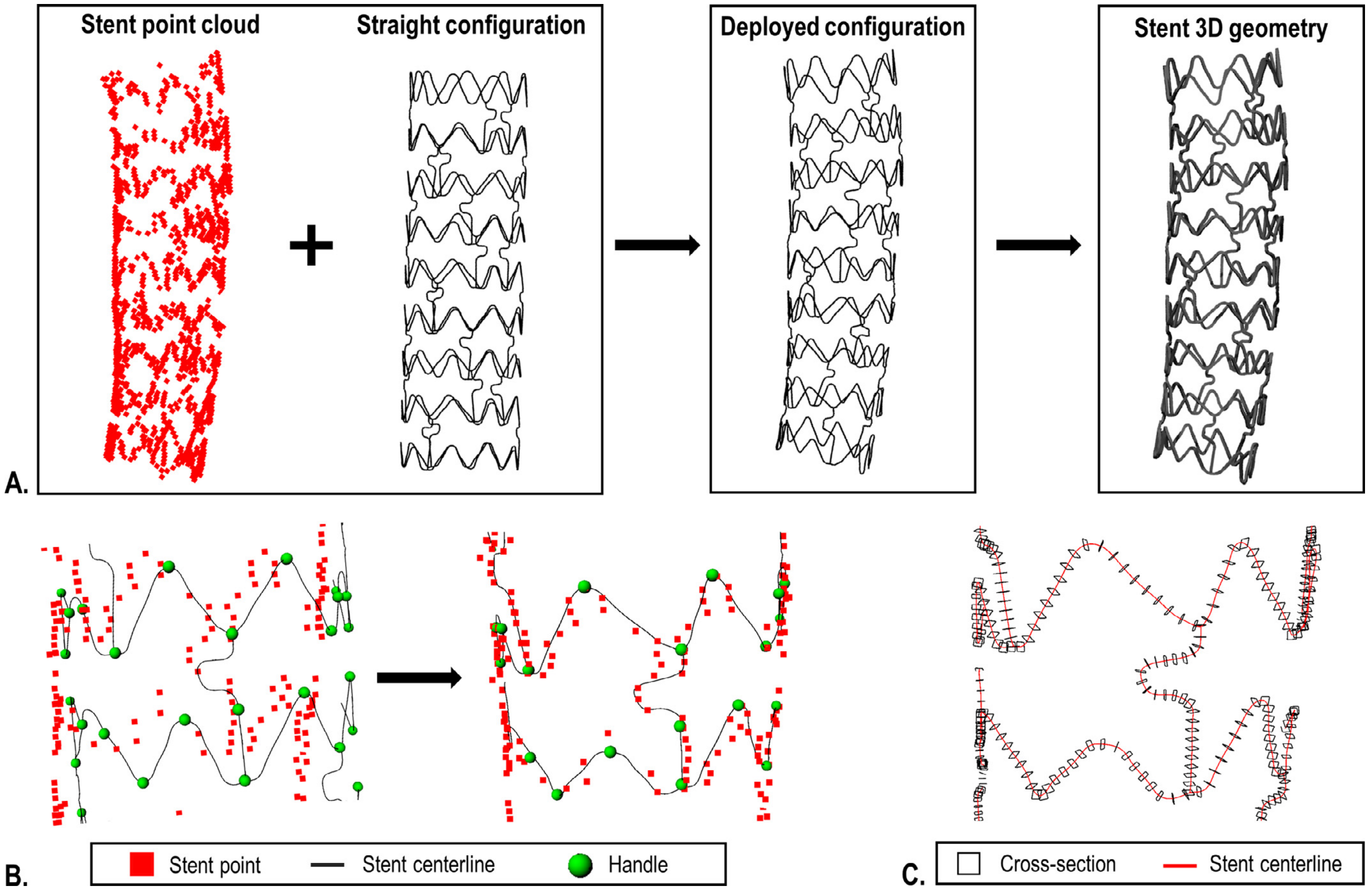

Fig. 6. Procedure used to create the 3D model of the stent. (A) The stent point cloud, obtained from OCT, and the straight configuration of the stent centerline, obtained from μCT, were used to generate deployed configuration of the centerline and subsequently the stent geometry. (B) Morphing of stent centerline through handles that were moved so that their distances with selected stent points were minimized. (C) Positioning of stent strut cross-sections were positioned along the morphed stent centerline for curve lofting.

Fig. 7. Three-dimensional geometry provided by the proposed method. The arrow indicates the direction of the simulated blood flow.

to the arterial and stent walls, which were defined as rigid. Blood was modeled as an incompressible, non-Newtonian fluid using the Carreau model [35]. Blood density was set to 1060 kg/m^3 [35]. The assumption of laminar flow was made as the maximum Reynolds number was ~157 at peak diastole. Solver settings are reported elsewhere [33].

3. Results

3.1. Validation of the segmentation algorithm

The Kruskal–Wallis test proved no statistical differences between lumen areas computed with the automatic and manual methods ($p > 0.05$). Linear regressions reported strong correlation between area values, resulting in correlations coefficients of 0.999 ($p < 0.005$) for all the combinations considered (i.e. algorithm vs. reader 1, algorithm vs. reader 2 and reader 1 vs. reader 2) (Fig. 8). The regression equations supported a significant linearity between datasets [36].

The Bland–Altman diagrams of the agreement between sets of lumen area values are reported in Fig. 9. The diagrams showed that the distribution of the differences in the lumen area values did not depend on the mean of the measurements among datasets. These distributions featured a mean of 0.29 mm^2 for the comparison ‘automatic against reader 1′, a mean of 0.26 mm^2 for the comparison ‘automatic against reader 2′, and a mean of −0.03 mm^2 for the inter-observer comparison. The 95% of the differences in lumen areas lied between −0.04 mm^2 and 0.61 mm^2 for the comparison ‘automatic against reader 1′, 0.032 mm^2 and 0.49 mm^2 for the comparison ‘automatic against reader 2, and −0.41 mm^2 and 0.36 mm^2 for the inter-observer comparison, respectively. The resultant biases in the Bland–Altman diagrams corresponded to relative errors in lumen area values of 3.42% (Fig. 9A), 3.15% (Fig. 9B), and 0.31% (Fig. 9C) with respect to the median area values of the

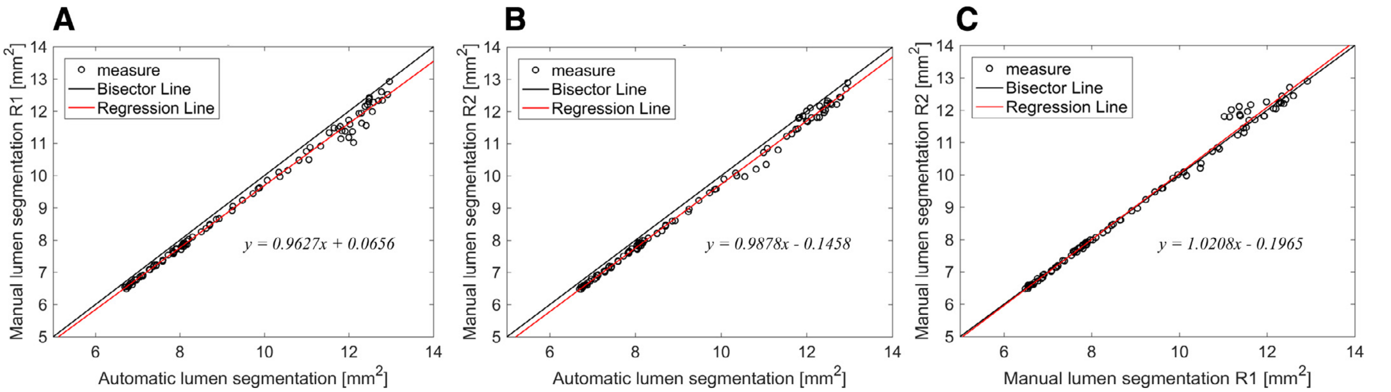

Fig. 8. Linear regression of lumen areas. (A) Automatic segmentation against manual segmentation made by reader 1. (B) Automatic segmentation against manual segmentation made by reader 2. (C) Inter-observer linear regression.

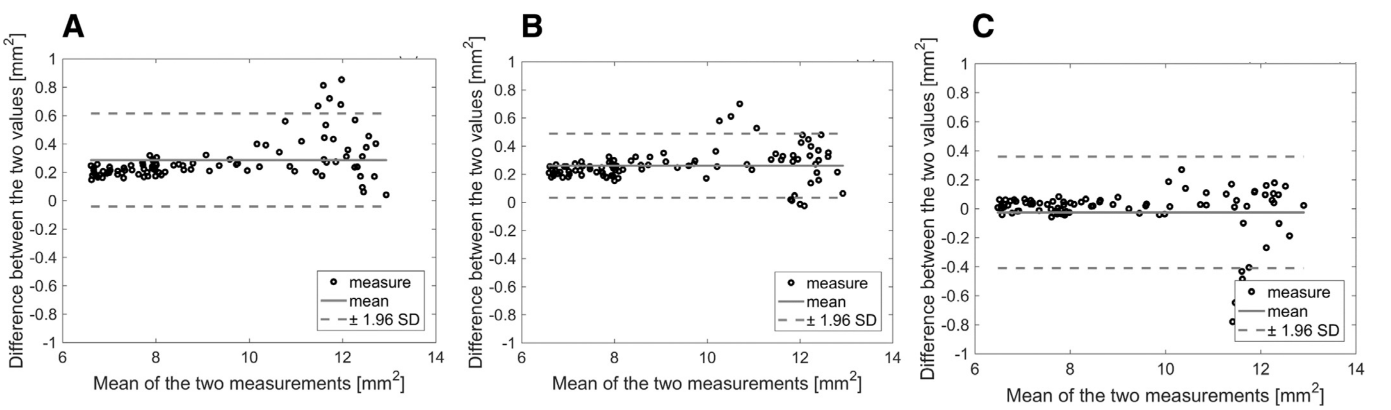

Fig. 9. Bland–Altman diagrams of lumen areas. (A) Automatic segmentation against reader 1 segmentation. (B) Automatic segmentation against reader 2 segmentation. (C) Inter-observer agreement study.

Table 1
Similarity indices for the segmentation of lumen and stent that were obtained from the indicated comparisons.

	Sensitivity (%)	Specificity (%)	Jaccard index (%)	Dice index (%)
Lumen				
Auto vs. R1	96.8 ± 1.2	99.6 ± 0.1	96.5 ± 1.2	98.2 ± 0.7
Auto vs. R2	96.8 ± 0.8	99.9 ± 0.1	96.4 ± 0.9	98.2 ± 0.5
R1 vs R2	98.9 ± 0.4	99.8 ± 0.3	97.6 ± 1.5	98.8 ± 0.8
Stent				
Auto vs. R1	91.7 ± 13.2	77.8 ± 28.2	78.1 ± 17.7	86.5 ± 12.8
Auto vs. R2	93.5 ± 12.3	72.9 ± 33.6	77.6 ± 18.6	86.0 ± 13.6
R1 vs. R2	96.5 ± 7.8	89.4 ± 18.0	89.2 ± 13.7	93.6 ± 9.0

Auto, automatic detection algorithm; R1, image reader 1; R2, image reader 2.

reference region-of-interest. The similarity indexes evaluated from comparison between datasets are reported in Table 1.

The Kruskal–Wallis for the detected number of stent struts reported no statistical differences between datasets ($p > 0.05$). The Bland–Altman diagrams for the LOA are shown in Fig. 10. These diagrams featured a mean of −17.43 µm, −17.73 µm, and −0.13 µm for the comparisons ‘automatic against reader 1′, ‘automatic against reader 2′ and ‘reader 1 against reader 2′, respectively.

The 95% of the differences in LOA lied respectively between −41.83 µm and 36.01 µm for the comparison ‘automatic against reader 1′, −43.37 µm and 36.85 µm for the comparison ‘automatic against reader 2′, lastly −25.01 µm and 24.74 µm for the inter-observer comparison. The similarity indices evaluated from comparison between datasets are reported in Table 1.

3.2. Validation of the alignment and orientation method

Figs. 11A and B show the superimposition between the 3D lumen geometry reconstructed with the OCT-based method and the reference geometry obtained from µCT. The percent difference in area between the OCT and µCT lumen reconstructions was 17.5%. As highlighted by the lumen cross-sections of Fig. 11A, the best coincidence between the lumen geometries was observed in the central region close to the SB used as the landmark for twist angle estimation. The relative error of the lumen volume between OCT and µCT lumen reconstructions was 7.1%. In addition, a qualitative comparison between reconstructed 3D models with stent is reported in Fig. 11C and shows satisfactory geometrical consistency.

Please cite this article as: S. Migliori et al., A framework for computational fluid dynamic analyses of patient-specific stented coronary arteries from optical coherence tomography images, Medical Engineering and Physics (2017), http://dx.doi.org/10.1016/j.medengphy.2017.06.027

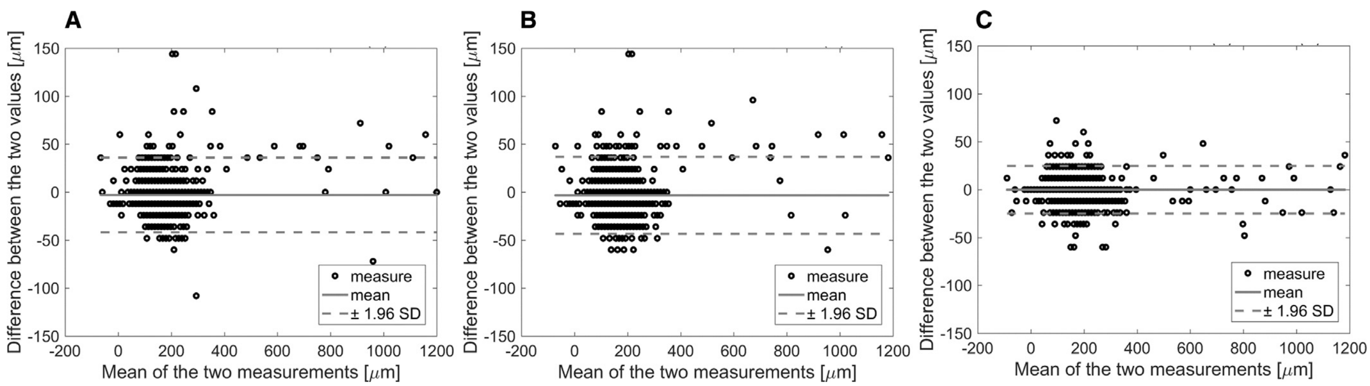

Fig. 10. Bland–Altman diagram of stent apposition (LOA). (A) Automatic segmentation against reader 1 segmentation. (B) Automatic segmentation against reader 2 segmentation. (C) Inter-observer agreement study.

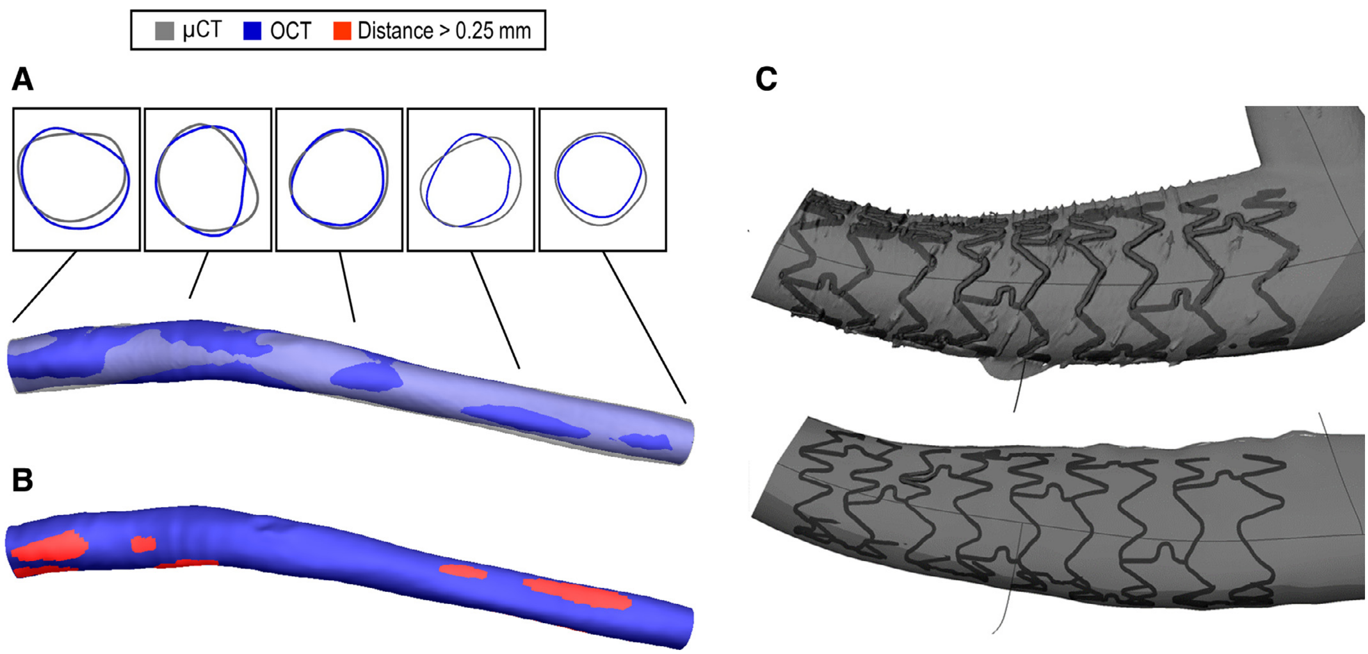

Fig. 11. Comparison between the 3D reconstruction obtained using the OCT-based method and the 3D reference model reconstructed from μCT. (A) Superimposition of the 3D lumen geometries provided by OCT (blue) and μCT (gray) data. (B) Regions of the OCT vessel geometry exhibiting distances from the μCT reference greater than 0.25 mm. (C) Qualitative comparison between the 3D stent geometry reconstructed from μCT (top) and that reconstructed with the OCT-based reconstruction method (bottom). (For interpretation of the references to colour in this figure legend, the reader is referred to the web version of this article.)

The distribution of the total distances between points of the stents is reported in Fig. 12. The 25th, 50th, and 75th quantiles of the total distances were 136.93 μm, 198.75 μm and 283.46 μm, respectively.

3.3. CFD simulation

Fig. 13A shows the contour map of time-averaged wall shear stress (TAWSS) along the MB wall. The distal portion was characterized by higher values of TAWSS, which was in agreement with the reduced dimension of the lumen cross-section compared to the proximal segment. The region with low TAWSS (i.e. TAWSS $\leq$ 0.4 Pa), recognized as critical for the occurrence of ISR [37], was confined to the stent region. The percentage area of the stented MB portion exposed to low TAWSS was 48.2%. Velocity contours with in-plane velocity streamlines are depicted at two selected locations at peak flow-rate in Fig. 13B and C. Velocity streamlines highlighted a disturbed flow at regions with stent malapposition.

4. Discussion

The influence of coronary artery anatomy on PCI outcomes is widely confirmed [3,26]. The application of medical imaging techniques, alongside the most advanced computational tools, can indicate possible disturbed hemodynamics in a specific clinical case. The occurrence of ISR is mainly related to hemodynamics, such as altered distribution of wall shear stress and regions of flow recirculation or stagnation due to stent deployment. In this study, a semi-automatic method was proposed to reconstruct a stented coronary artery from OCT images in order to carry out CFD analyses. This method was applied on a rigid phantom that resembled a segment of LAD coronary artery with multiple bifurcations. The accuracy of this method was assessed through a quantitative validation of the fully-automatic image segmentation algorithm and the semi-automatic 3D geometry reconstruction of the coronary phantom with an implanted stent.

Several works in the literature propose methods that use intravascular imaging techniques to automatically reconstruct the lumen geometry, such as in [10,11,14,15,17,26,38–41]. However, the

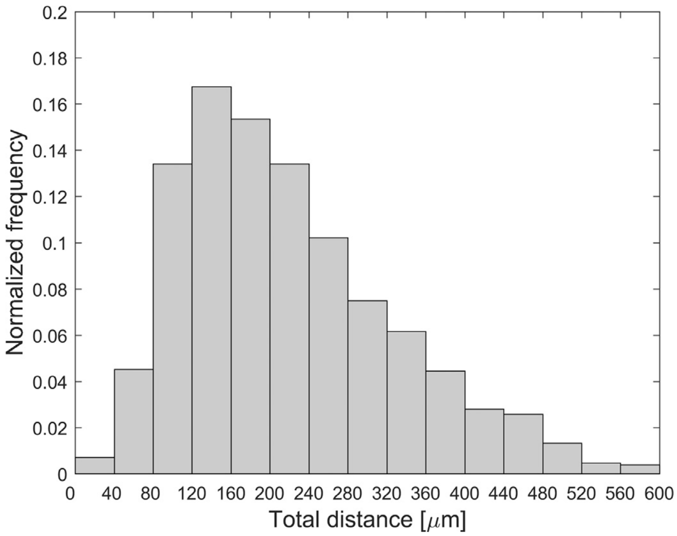

Fig. 12. Histogram of the total distances between centerline points of the stents reconstructed using the OCT-based method and those provided by µCT data.

literature lacks of exhaustive analyses about coherence with actual lumen and stent geometries. This work as well as the studies by Chiastra et al. [42] and O'Brien et al. [43] propose a framework for the reconstruction of 3D artery geometries including the implanted stent starting from OCT images for the execution of CFD simulations. Specifically, in this study the stent geometry was better preserved through the usage of handles on the implanted device centerline for the morphing procedure, even where the position of stent struts was unknown due to light reflection on the OCT guidewire. Moreover, the proposed methodology was quantitatively validated to elucidate the limitations correlated to the segmentation and the 3D geometry reconstruction, which proved satisfactorily accurate. Therefore, this work represents an important contribution for the development of a reliable reconstruction tool for the evaluation of altered hemodynamics following stent deployment.

Results showed that the segmentation algorithm correctly identified the lumen contours and provided a good stent identification. Indeed, similarity indexes for the lumen were close to 100% considering the manual segmentation performed by the two image readers. In fact, the sets of computed lumen areas had strong linear correlations and good agreement. The resultant biases in the Bland–Altman diagrams were ~3% of the lumen areas from manual segmentation and were comparable to values reported in previous studies [30,44,45]. Ranges with the 95% of the differences in lumen areas were smaller than those obtained in the works by Celi and Berti (i.e. $-1.2\,\text{mm}^2$ and $1.2\,\text{mm}^2$) [45] and Chatzizisis et al. (i.e. $-1.6\,\text{mm}^2$ and $1.3\,\text{mm}^2$) [26]. The similarity indexes for stent segmentation reported good stent detection. The average sensitivity of the algorithm for stent segmentation was in agreement with the work of Wang et al. (i.e. 94%) [27]. The Bland–Altman diagrams for LOA reported no significant bias and smaller limits of agreement than those found by Ughi et al. (i.e. 80–85 µm) [31].

The alignment and orientation procedure provided reliable 3D reconstruction of phantom MB and stent. In particular, discrepancies between lumen surfaces were larger distally to the reference SB due to the axial twist angle. Indeed, reference points in that vessel portion (i.e. bifurcation points) were hardly detectable for the estimation of the twist angle. Similar observations hold true for the stent reconstruction, since stent centroids were processed with the same alignment algorithm as the points belonging to the lumen contours. The median of total distances between the reconstructed stent centerline and the reference was comparable to twice the strut thickness.

The obtained 3D geometry allowed a successful CFD analysis. The local hemodynamics was investigated in a high fidelity geometry with respect to the real one, which allowed us to distinguish apposed and malapposed stent struts as in the real case. Indeed, the considered hemodynamic indexes were in agreement with previous computational studies on image-based stented coronary arteries [17,18,33]. In particular, adverse values of TAWSS were located at stent struts and disturbed blood flow structures were caused by stent malapposition.

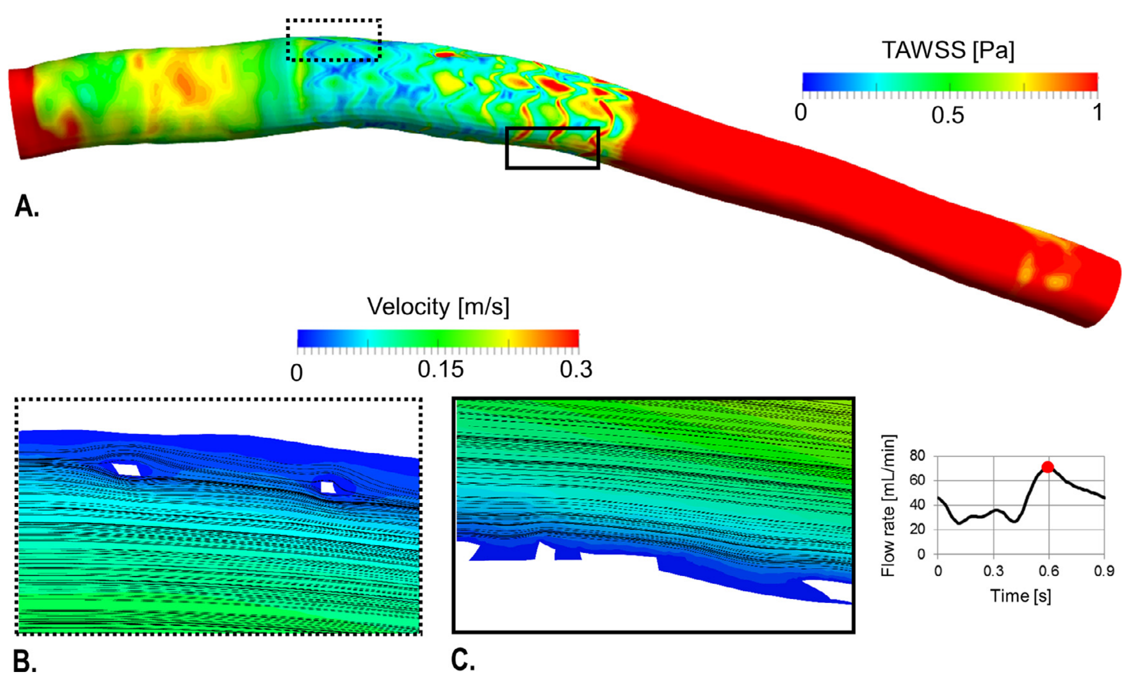

Fig. 13. Results of the CFD analysis. (A) Contour plot of time-averaged wall shear stress (TAWSS). (B) Velocity contour with in-plane velocity streamlines at peak flow-rate at a cross-section characterized by malapposed struts. (C) Velocity contour with in-plane velocity streamlines at peak flow-rate at a cross-section with apposed struts.

Please cite this article as: S. Migliori et al., A framework for computational fluid dynamic analyses of patient-specific stented coronary arteries from optical coherence tomography images, Medical Engineering and Physics (2017), http://dx.doi.org/10.1016/j.medengphy.2017.06.027

In general, the framework proposed in this study showed promising results concerning the accuracy of the 3D vessel reconstruction and the feasibility of CFD analyses with the corresponding geometry. The fundamental contribution of the described methodology is the reconstruction of a patient-specific stented coronary artery through images that are routinely acquired during PCI. The resultant high fidelity geometry allows one to evaluate local hemodynamics alterations within coronary arteries after stent deployment, with outcomes that are peculiar to each clinical case. Therefore, the presented framework might be used by cardiologists as a tool during both pre-operative planning phase and post-operative follow-up windows, providing a knowledge of the most prone regions to ISR due to adverse WSS along the endothelium.

Although results supported the reliability of the presented framework, there are a number of limitations. The developed reconstruction method was applied to a rigid phantom made of a polymeric material. Therefore, the OCT acquisition was not performed in nominal conditions and the images featured a higher brightness as compared to in vivo acquisitions. However, in authors' opinion the image segmentation outcomes are hardly influenced because the automatic algorithm is based on grayscale gradients in each OCT frame. Second, it was impossible to use the two proximal SBs as landmark to improve the reconstruction because of the impossibility to clearly distinguish those from the MB at the bifurcation carina. Third, the assumption made to sample the MB centerline according to the distance between OCT frames might compromise the accuracy when a vessel with significant tortuosity is reconstructed. Indeed, in those cases the alignment should be performed along the path followed by the OCT catheter during pullback. Fourth, the OCT images underwent several elaborations that might have affected the final reconstruction. Nevertheless, overall results from the validation procedure suggest that such elaborations had a limited influence on the final reconstruction compared to the assumptions made for the alignment procedure. Lastly, the implemented algorithm for stent strut detection is not applicable to bioresorbable stents, since OCT images do not present the same features (i.e. black trailing shadows behind high intensity pixels) as when the implanted device is made of a metallic material.

5. Conclusions

This study presented a semi-automatic method to reconstruct the actual configuration of coronary arteries after stent implantation from OCT images. The algorithm was applied to a rigid phantom that resembled a segment of LAD with bifurcations and was used to acquire OCT images after stent deployment.

The fully automatic OCT segmentation procedure was validated against manual segmentation and provided good results as confirmed by high values of similarity indices and correlation coefficients. The obtained 3D reconstruction of the stented phantom was compared with the geometry reconstructed from μCT scan, used as ground truth, demonstrating the incidence of distortion from catheter-based imaging techniques.

Finally, the 3D reconstruction was successfully used to investigate the local hemodynamics. The good outcomes obtained from the validation procedure enable to state that the proposed reconstruction methodology is a promising tool for CFD analyses also in patient-specific stented geometries.

Conflict of interest

The authors have no professional or financial conflicts of interest to disclose.

Ethical approval

This study did not involve any human or animal subjects, therefore ethical approval was not required.

Acknowledgments

Susanna Migliori is supported by the European Commission through the H2020 Marie Skłodowska-Curie European Training Network H2020-MSCA-ITN-2014 VPH-CaSE, www.vph-case.eu, GA No. 642612. Marinella Levi and Caterina Credi from the +LAB of the Department of Chemistry, Materials and Chemical Engineering 'Giulio Natta' of Politecnico di Milano are greatly acknowledged for printing the 3D coronary phantom.

References

[1] Puddu PE, Menotti A. Coronary heart disease differences in Eastern versus Western Europe: a demanding situation. Int J Cardiol 2016;217:S60–3. doi:10.1016/j.ijcard.2016.06.225.
[2] Mozaffarian D, Benjamin EJ, Go AS, Arnett DK, Blaha MJ, Cushman M, et al. Heart disease and stroke statistics—2016 update: a report from the American Heart Association. Circulation 2016;133:e38–360. doi:10.1161/CIR.0000000000000350.
[3] Lassen JF, Holm NR, Banning A, Burzotta F, Lefèvre T, Chieffo A, et al. Percutaneous coronary intervention for coronary bifurcation disease: 11th consensus document from the European Bifurcation Club. EuroIntervention 2016;12:38–46. doi:10.4244/EIJV12I1A7.
[4] Mintz GS. Intravascular imaging of coronary calcification and its clinical implications. JACC Cardiovasc Imaging 2015;8:461–71. doi:10.1016/j.jcmg.2015.02.003.
[5] Madhavan MV, Tarigopula M, Mintz GS, Maehara A, Stone GW, Généreux P. Coronary artery calcification: pathogenesis and prognostic implications. J Am Coll Cardiol 2014;63:1703–14. doi:10.1016/j.jacc.2014.01.017.
[6] Antoniadis AP, Mortier P, Kassab G, Dubini G, Foin N, Murasato Y, et al. Biomechanical modeling to improve coronary artery bifurcation stenting: expert review document on techniques and clinical implementation. JACC Cardiovasc Interv 2015;8:1281–96. doi:10.1016/j.jcin.2015.06.015.
[7] Edelman ER, Rogers C. Pathobiologic responses to stenting. Am J Cardiol 1998;81 4E-6E. doi:10.1016/S0002-9149(98)00189-1.
[8] Van der Heiden K, Gijsen FJ, Narracott A, Hsiao S, Halliday I, Gunn J, et al. The effects of stenting on shear stress: relevance to endothelial injury and repair. Cardiovasc Res 2013;99:269–75. doi:10.1093/cvr/cvt090.
[9] LaDisa JF Jr, Hettrick DA, Olson LE, Guler I, Gross ER, Kress TT, et al. Stent implantation alters coronary artery hemodynamics and wall shear stress during maximal vasodilation. J Appl Physiol 2002;93:1939–46. doi:10.1152/japplphysiol.00544.2002.
[10] Zaromytidou M, Siasos G, Coskun AU, Lucier M, Antoniadis AP, Papafaklis MI, et al. Intravascular hemodynamics and coronary artery disease: new insights and clinical implications. Hell J Cardiol 2016;57:389–400. doi:10.1016/j.hjc.2016.11.019.
[11] Toutouzas K, Chatzizisis YS, Riga M, Giannopoulos A, Antoniadis AP, Tu S, et al. Accurate and reproducible reconstruction of coronary arteries and endothelial shear stress calculation using 3D OCT: comparative study to 3D IVUS and 3D QCA. Atherosclerosis 2015;240:510–19. doi:10.1016/j.atherosclerosis.2015.04.011.
[12] Wahle A, Prause PM, DeJong SC, Sonka M. Geometrically correct 3-D reconstruction of intravascular ultrasound images by fusion with biplane angiography — methods and validation. IEEE Trans Med Imaging 1999;18:686–99.
[13] Çimen S, Gooya A, Grass M, Frangi AF. Reconstruction of coronary arteries from X-ray angiography: a review. Med Image Anal 2016;32:46–68. doi:10.1016/j.media.2016.02.007.
[14] Bezerra HG, Costa MA, Guagliumi G, Rollins AM, Simon DI. Intracoronary optical coherence tomography: a comprehensive review. JACC Cardiovasc Interv 2009;2:1035–46. doi:10.1016/j.jcin.2009.06.019.
[15] Nammas W, Ligthart JM, Karanasos A, Witberg KT, Regar E. Optical coherence tomography for evaluation of coronary stents *in vivo*. Expert Rev Cardiovasc Ther 2013;11:577–88. doi:10.1586/erc.13.37.
[16] Regar E, Ligthart J, Bruining N, van Soest G. The diagnostic value of intracoronary optical coherence tomography. Herz 2011;36:417–29. doi:10.1007/s00059-011-3487-7.
[17] Ellwein LM, Otake H, Gundert TJ, Koo BK, Shinke T, Honda Y, et al. Optical coherence tomography for patient-specific 3D artery reconstruction and evaluation of wall shear stress in a left circumflex coronary artery. Cardiovasc Eng Technol 2011;2:212–27. doi:10.1007/s13239-011-0047-5.
[18] Chiastra C, Wu W, Dickerhoff B, Aleiou A, Dubini G, Otake H, et al. Computational replication of the patient-specific stenting procedure for coronary artery bifurcations: from OCT and CT imaging to structural and hemodynamics analyses. J Biomech 2016;49:2102–11. doi:10.1016/j.jbiomech.2015.11.024.
[19] Bourantas CV, Kourtis IC, Plissiti ME, Fotiadis DI, Katsouras CS, Papafaklis MI, et al. A method for 3D reconstruction of coronary arteries using biplane an-

giography and intravascular ultrasound images. Comput Med Imaging Graph 2005;29:597–606. doi:10.1016/j.compmedimag.2005.07.001.
[20] Montin E, Migliori S, Chiastra C, Credi C, Fedele R, Aurigemma C, et al. A method for coronary bifurcation centerline reconstruction from angiographic images based on focalization optimization. In: 2016 38th annual international conference of the IEEE engineering in medicine and biology society. IEEE; 2016. p. 4165–8. doi:10.1109/EMBC.2016.7591644.
[21] Fedele R, Ciani A, Galantucci L, Bettuzzi M, Andena L. A regularized, pyramidal multi-grid approach to global 3D-volume digital image correlation based on X-ray micro-tomography. Fundam Informaticae 2013;125:361–76. doi:10.3233/FI-2013-869.
[22] Fedele R, Ciani A, Fiori F. X-ray microtomography under loading and 3D-volume digital image correlation. A review. Fundam Informaticae 2014;135:171–97. doi:10.3233/FI-2014-1117.
[23] Fedele R, Galantucci L, Ciani A. Global 2D digital image correlation for motion estimation in a finite element framework: a variational formulation and a regularized, pyramidal, multi-grid implementation. Int J Numer Methods Eng 2013;96:739–62. doi:10.1002/nme.4577.
[24] Chiastra C, Montin E, Bologna M, Migliori S, Aurigemma C, Burzotta F, et al. Reconstruction of stented coronary arteries from optical coherence tomography images: feasibility, validation, and repeatability of a segmentation method. PLoS One 2017;12:e0177495. doi:10.1371/journal.pone.0177495.
[25] Gonzalez RC, Woods RE, Eddins SL. Digital image processing using Matlab - Gonzalez Woods & Eddins.pdf. Education 2004;624:609. doi:10.1117/1.3115362.
[26] Chatzizisis YS, Koutkias VG, Toutouzas K, Giannopoulos A, Chouvarda I, Riga M, et al. Clinical validation of an algorithm for rapid and accurate automated segmentation of intracoronary optical coherence tomography images. Int J Cardiol 2014;172:568–80. doi:10.1016/j.ijcard.2014.01.071.
[27] Wang A, Eggermont J, Dekker N, Garcia-Garcia HM, Pawar R, Reiber JHC, et al. Automatic stent strut detection in intravascular optical coherence tomographic pullback runs. Int J Cardiovasc Imaging 2013;29:29–38. doi:10.1007/s10554-012-0064-y.
[28] Bourantas C, Fotiadis DI, Kourtis IC, Michalis LK, Plissiti M. Three-dimensional coronary artery reconstruction using fusion of intravascular ultrasound and biplane angiography. Int Congr Ser 2003;1256:1133–8. doi:10.1016/S0531-5131(03)00334-0.
[29] Martin Bland J, Altman D. Statistical methods for assessing agreement between two methods of clinical measurement. Lancet 1986;327:307–10. doi:10.1016/S0140-6736(86)90837-8.
[30] de Macedo MMG, Takimura CK, Lemos PA, Gutierrez MA. A robust fully automatic lumen segmentation method for in vivo intracoronary optical coherence tomography. Revista Brasileira de Engenharia Biomedica 2016;32:35–43. http://dx.doi.org/10.1590/2446-4740.0759.
[31] Ughi GJ, Adriaenssens T, Onsea K, Kayaert P, Dubois C, Sinnaeve P, et al. Automatic segmentation of in-vivo intra-coronary optical coherence tomography images to assess stent strut apposition and coverage. Int J Cardiovasc Imaging 2012;28:229–41. doi:10.1007/s10554-011-9824-3.
[32] Davies JE, Whinnett ZI, Francis DP, Manisty CH, Aguado-Sierra J, Willson K, et al. Evidence of a dominant backward-propagating "suction" wave responsible for diastolic coronary filling in humans, attenuated in left ventricular hypertrophy. Circulation 2006;113:1768–78. doi:10.1161/CIRCULATIONAHA.105.603050.
[33] Chiastra C, Morlacchi S, Gallo D, Morbiducci U, Cárdenes R, Larrabide I, et al. Computational fluid dynamic simulations of image-based stented coronary bifurcation models. J R Soc Interface 2013;10:20130193. doi:10.1098/rsif.2013.0193.
[34] Kessler W, Moshage W, Galland A, Zink D, Achenbach S, Nitz W, et al. Assessment of coronary blood flow in humans using phase difference MR imaging. Comparison with intracoronary Doppler flow measurement. Int J Card Imaging 1998;14:179–86.
[35] Caputo M, Chiastra C, Cianciolo C, Cutrì E, Dubini G, Gunn J, et al. Simulation of oxygen transfer in stented arteries and correlation with in-stent restenosis. Int J Numer Methods Biomed Eng 2013;29:1373–87. doi:10.1002/cnm.2588.
[36] Giavarina D. Understanding Bland Altman analysis. Biochem Med 2015;25:141–51. doi:10.11613/BM.2015.015.
[37] Malek AM, Alper SL, Izumo S. Hemodynamic shear stress and its role in atherosclerosis. JAMA 1999;282:2035–42. doi:10.1001/jama.282.21.2035.
[38] Bourantas CV, Papafaklis MI, Athanasiou L, Kalatzis FG, Naka KK, Siogkas PK, et al. A new methodology for accurate 3-dimensional coronary artery reconstruction using routine intravascular ultrasound and angiographic data: Implications for widespread assessment of endothelial shear stress in humans 2013. EuroIntervention 2013;9:582–93. doi:10.4244/EIJV9I5A94.
[39] Papafaklis MI, Bourantas CV, Yonetsu T, Vergallo R, Kotsia A, Nakatani S, et al. Anatomically correct three-dimensional coronary artery reconstruction using frequency domain optical coherence tomographic and angiographic data: head-to-head comparison with intravascular ultrasound for endothelial shear stress assessment in humans. EuroIntervention 2015;11:407–15. doi:10.4244/EIJY14M06_11.
[40] Wentzel JJ, Chatzizisis YS, Gijsen FJH, Giannoglou GD, Feldman CL, Stone PH. Endothelial shear stress in the evolution of coronary atherosclerotic plaque and vascular remodelling: current understanding and remaining questions. Cardiovasc Res 2012;96:234–43. doi:10.1093/cvr/cvs217.
[41] Slager CJ, Wentzel JJ, Schuurbiers JCH, Oomen JAF, Kloet J, Krams R, et al. True 3-dimensional reconstruction of coronary arteries in patients by fusion of angiography and IVUS (ANGUS) and its quantitative validation. Circulation 2000;102:511–16.
[42] Chiastra C, Montin E, Burzotta F, Mainardi L, Migliavacca F. Coronary stenting: from optical coherence tomography to fluid dynamic simulations. In: 13th IEEE international conference on bioinformatics and bioengineering; 2013. p. 1–4. doi:10.1109/BIBE.2013.6701699.
[43] O'Brien CC, Kolandaivelu K, Brown J, Lopes AC, Kunio M, Kolachalama VB, et al. Constraining OCT with knowledge of device design enables high accuracy hemodynamic assessment of endovascular implants. PLoS One 2016;11:e0149178. doi:10.1371/journal.pone.0149178.
[44] Chatzizisis YS, Koutkias VG, Toutouzas K, Giannopoulos A, Chouvarda I, Riga M, et al. Clinical validation of an algorithm for rapid and accurate automated segmentation of intracoronary optical coherence tomography images. Int J Cardiol 2014;172:568–80. doi:10.1016/j.ijcard.2014.01.071.
[45] Celi S, Berti S. In-vivo segmentation and quantification of coronary lesions by optical coherence tomography images for a lesion type definition and stenosis grading. Med Image Anal 2014;18:1157–68. doi:10.1016/j.media.2014.06.011.